Electrochemical Potential-Dependent Stability and Activity of MoS 3 during the Hydrogen Evolution Reaction

Nawras Abidi, Amit Sahu, Pascal Raybaud, Stephan Steinmann

Electrochemical potential-dependent stability and activity of MoS_3 during the hydrogen evolution reaction

Nawras Abidi,[†] Amit Sahu,[†] Pascal Raybaud,[*,‡,†] and Stephan N. Steinmann[*,†]

†*Univ Lyon, Ens de Lyon, CNRS UMR 5182, Université Claude Bernard Lyon 1, Laboratoire de Chimie, F69342, Lyon, France*

‡*IFP Energies nouvelles, Rond-point de l'échangeur de Solaize, 69360 Solaize, France*

E-mail: raybaud@ifpen.fr; stephan.steinmann@ens-lyon.fr

Phone: (+33)4 72 72 81 55

Abstract

Amorphous $a-MoS_3$ is an appealing low-cost catalyst for the hydrogen evolution reaction (HER), a promising process for electrocatalytic hydrogen generation. In this study, we scrutinize the stability and HER catalytic activity of carbon supported Mo_3S_{9-x}-clusters under electrochemical conditions using Grand-Canonical Density Functional Theory (DFT) coupled with a cluster-continuum solvation strategy. We show that some sulfur atoms of Mo_3S_9 cluster can be removed as H_2S under HER conditions. This partial desulfurization leads to a stable working state Mo_3S_8 or Mo_3S_7 with HER catalytic activity at moderate thermodynamic overpotentials. The desulfurization process simultaneously induces water adsorption on undercoordinated molybdenum sites. The so formed hydrated Mo_3S_{9-x}-clusters can exhibit two distinct active sites. On $Mo_3S_8(H_2O)_2$, the top SH* species are active for HER, whereas OH* species are involved in HER on $Mo_3S_7(H_2O)_3$. By comparison with a previous study of the

HER catalyzed by 2H-MoS_2 edge sites, we demonstrate that S-defective $a-MoS_3$ is an efficient HER electrocatalyst. Moreover, in contrast to active sites on 2H-MoS_2, the HER mechanism on Mo_3S_{9-x}-clusters involves a protonation step, instead of the common proton coupled electron transfer, an elementary reaction step that required GC-DFT to be identified.

Keywords

MoS_3, hydrogen evolution reaction, grand-canonical density functional theory, proton coupled electron transfer, MoS_2

1 Introduction

The development of environment-friendly, renewable, and affordable energy solutions that can meet the global energy demand without carbon emissions is an acute and important issue for our society. Solar, wind, hydraulic, and other renewable energy sources are promising carbon-neutral alternatives to fossil fuels, but are often intermittent and require large-scale storage to be suitable for grid integration.[1] Hydrogen (H_2) is considered as an ideal energy vector due to its high energy density and non-toxic combustion products. Furthermore, H_2 has various applications in the production of basic chemicals such as ammonia, in the transformation of organic molecules[2,3] but also in fuel cells and hydrogen internal combustion engine vehicles[4]. Currently, hydrogen is mostly produced through methane steam reforming and coal gasification, which implies a high energy consumption and emits significant amounts of carbon dioxide.[5,6] One of the most environment-friendly alternatives for the production of H_2 is the electrolysis of water, where the hydrogen evolution reaction (HER) occurs at the cathode.[7,8] Platinum is recognized as the most efficient HER electrocatalyst due to its high chemical and corrosion resistance and low overpotential.[9] However, its scarcity and high cost encourage research for identifying Earth-abundant electrocatalysts that could be produced on a large scale.

Non-noble transition metal-based materials have emerged as promising catalysts for HER, in particular as Mo/W-disulfides, Fe, Co, Ni sulfides, and metal carbides, phosphides, or selenides.[7] MoS_2 has shown significant HER catalytic activity but the activity remains limited to minimally exposed active edge sites as the basal plane is largely inactive towards HER.[10] A variety of approaches have been implemented to achieve active site-rich MoS_2 by doping or the creation of defects.[7] Beyond crystalline MoS_2, amorphous-MoS_x with $x \approx 3$ has also gained considerable attention in recent years.[11] Furthermore, in a comparative study of amorphous MoS_3 and MoS_2, MoS_3 was observed to exhibit higher HER activity and also increased stability towards a wide range of pHs.[12,13] Several explanations have been proposed. On the one hand, due to its lower crystallinity, MoS_3 might expose more accessible HER

active sites compared to MoS_2, which then would explain the higher catalytic activity (when normalized per Mo atom).[14] On the other hand, the nature of the active sites may differ in amorphous MoS_3 and MoS_2.

Due to its amorphous nature and the inherent complexity of obtaining an atomic scale description of electrocatalytic interfaces, the nature of the active sites of a-MoS_3 in HER is widely debated.[15–19] By X-ray photoelectron spectroscopy (XPS) and density functional theory (DFT) calculations, it was proposed that MoS_2-edge-like sites exposing S^{2-} monomers would be responsible for the HER activity of a-MoS_3,[16] while top S_2^{2-} species are also observed to be good proton acceptor sites by X-ray adsorption spectroscopy.[17] Other XPS observations suggested that both bridging S_2^{2-} and top S^{2-} are the primary sources of HER activity in in amorphous MoS_3.[20] The importance of bridging S_2^{2-} species as active sites has also been supported by operando Raman spectroscopic measurements and DFT calculations.[18] By contrast, undercoordinated Mo-centers might also give rise to Mo-hydride intermediates involved in HER.[15] Moreover, all these active sites might interconvert as suggested by in situ Raman measurements: bridging S_2^{2-} species may convert into top S_2^{2-} species and can then create unsaturated Mo-sites.[19] DFT simulations of S-S vibrational frequencies for various neutral a-MoS_3 polymorphs[21] suggest that some of these interpretations might be considered with care, as they rely on a possibly misleading assignment of the top and bridging S_2^{2-} species in a-MoS_3 through infrared (IR) or Raman spectroscopies. Indeed, the complex structure of a-MoS_3 phase has been debated for many years.[22–25] The DFT study by Sahu et al. revealed that large sizes of neutral a-MoS_3 polymers favor distorted Mo chain-like structures, while smaller entities with Mo triangular moieties are more stable.[21] Such structural features are crucial for the identification of the nature of HER active sites.

A number of studies have been undertaken on well-defined thiomolybdate nanoclusters such as $[Mo_3S_{13}]^{2-}$ and $[Mo_3S_{12}]^{2-}$ which are often invoked "model" building blocks of a-MoS_3 or MoS_2 nanoclusters.[15,26–32] For instance, a DFT study revealed that the catalytic activity of bridging-S_2^{2-} in a-MoS_3 is higher than hollow S, which was confirmed by Raman

spectroscopy of $[Mo_3S_{13}]^{2-}$ clusters.[31] However, the reversed conclusion had been reached by an earlier study, leaving the question unsettled.[32] Along the same line, several experimental studies suggested that partially oxidized (a-$MoOS_3$) species could be even better for HER catalytic activity.[15,33,34] In the same spirit, Lopez et al. have shown that, depending on pH conditions, the unsaturated S, top S_2^{2-} species, and to some extent, sulfur deficient, oxygen containing Mo sites could be active sites for HER in a-MoS_3.[12]

Abidi et al. examined the stability of MoS_2-edges under electrochemical potential and evidenced possible HER mechanisms including edge reconstructions due to H_2S-release and involving OH-based HER active sites.[35] Moreover, in the context of the hydrodesulfurization catalyst preparation, small amorphous MoS_3 clusters are known to be intermediate species connecting the Mo oxide precursor to MoS_2 under sulfo-reduction conditions.[36,37] However, kinetic limitations could prevent the full sulfidation of such small Mo-clusters, so that some residual oxygen atoms may remain bonded to the Mo-sites.[36] Hence, in an aqueous environment, it may be critical to study the stability of Mo-sites in MoS_3 clusters with respect to H_2S-release and the impact of coordinating oxygen rather than sulfur atoms.

Considering this previous knowledge, we will investigate the HER mechanisms of a relevant MoS_3 model and its stability with respect to the release of H_2S. Since we aim at studying MoS_3 entities maximizing the number of potential active sites, we will consider a triangular $Mo_3S_{9\text{-}x}$ cluster model as determined in our previous work.[21] A conductive support such as glassy carbon, carbon nanotubes or carbon black is experimentally used to enhance the electron transfer required for HER.[14,38] Hence, we will use a model graphite support with a Stone-Wales defect as an anchoring point defect. Furthermore, to the best of our knowledge, our study is the first one going beyond pure in vacuo simulation of MoS_3. Here, we take into account the three following crucial parameters: (i) solvation via an implicit solvent, (ii) explicit H_2O/H_2S exchanges, (iii) explicit modelling of the impact of the electrochemical potential via grand-canonical DFT. As it will be shown, GC-DFT suggests that, depending on the coordination environment, these small molecular catalysts feature both coupled and

uncoupled proton-electron transfers which behave differently than MoS2 catalysts.

2 Methods

2.1 Computational details

The computations were performed by the Vienna ab initio simulation package (VASP).[39] We used the dispersion corrected Generalized Gradient Approximation density functional PBE-dDsC.[40,41] The Projector Augmented Waves method[42,43] was used with the standard pseudopotentials. The electronic density was calculated with a cutoff energy of 500 eV at the Γ point. The precision setting of VASP is set to "accurate", which increases the density of the numerical grids, and therefore the numerical precision, with respect to the default settings. A Fermi smearing corresponding to room temperature (0.025 eV) was used for all computations. The convergence criterion for the self-consistency process is set to 10^{-5} eV for the optimization of the wave function. The maximum forces are converged to 0.025 eV/Å during the geometry optimization.

We have simulated Mo_3S_{9-x} nanoclusters as a representative active site structure for small nanoparticles of MoS_3 (see Fig. 1a) as proposed in our previous study on a-MoS_3.[21] The Mo_3S_{9-x} nanoclusters are positioned on graphite support model at the location of a Stone-Wales defect, which has been introduced to mimic an anchoring point. Orientations of the nano-cluster were explored using DockOnSurf, specifying the Stone-Wales defect as the adsorption site and various sulfur atoms as anchoring points.[44] The most stable orientation of the nanocluster is presented in Fig. 1b.

We evaluate the electrocatalytic activity by explicitly considering the electrochemical potential via Grand Canonical DFT (GC-DFT) in combination with the linearized Poisson-Boltzmann equation as implemented in VASPsol.[45] The "critical" density ρ_c, defining the interface, is set to 0.00025 $e^-/\text{Å}^{-1}$ as in our previous studies[46,47] to prevent the implicit solvent from getting between the weakly bound carbon layers. To mimic the experimental

conditions of 0.5 M aqueous H_2SO_4 solutions, the Debey screening length is set to 3 Å, corresponding to a 1 M electrolyte. To properly define the work function (electrochemical potential) of the interface, we perform a symmetrization with respect to a plane for all structures, ensuring a zero net dipole moment of the slab. Given that VASPsol only implements 3D boundary conditions, both sides of the slab are solvated. For asymmetric, nominally charged systems, this can lead to artifacts, as demonstrated in ref.[48] Only the central layer is fixed in its bulk position and a vacuum of 20 Å is added at the top and bottom of the slab to ensure minimal interactions across unit-cells (See Fig. 1c). The large out-of-plane size of the unit cell ensures that the counter-charge added by the linearized Poisson-Boltzmann Equation drops to zero in the "bulk" solvent region.[49] The potential dependence is studied by varying the number of electrons and retrieving the corresponding potential (or, equivalently, workfunction). In practice, the system charge is varied from -1 to +1 in steps of 0.2 e^-. The system's electronic charge is neutralized via the Poisson-Boltzmann equation, similar to other Grand Canonical DFT schemes in the literature.[50–55] We then compute the grand potential via

$$G(U) \approx E(q) - \mu(q) \cdot q \tag{1}$$

Where $E(q)$ refers to the electronic energy of the system with charge q (q=0 corresponds to the neural system) as provided by the electronic structure code (with electrons coming from/going to their reference state in vacuum) and $\mu(q)$ being the corresponding workfunction. This formulation of the grand-potential goes back to the Legendre transform introduced by Nalewajski.[56]

The obtained relation between the grand-potential and the electrochemical potential is then fitted to an analytical formula, which is a parabola for conductors (see Fig. S1). To convert the absolute potentials obtained from DFT to the SHE scale, we use the recommended value of 4.44 V.[57] This approach has been used to elucidate reaction mechanisms at electrified interfaces[58,59] including the oxygen evolution reaction[60,61] and to fathom the

origin of electrochemical promotion of catalysis.[62,63]

2.2 Reaction energies

The *adsorption energy* ΔG_{ads} of different species are calculated according to the following formula:

$$\Delta G_{ads}(U) = \frac{1}{2} \times (G_{product}(U) - G_{reactant}(U) - G_{Rmol}(U)) \tag{2}$$

Here $G_{product}(U)$ and $G_{reactant}(U)$ are the potential-dependent energies of surfaces with and without an additional adsorbate, respectively. These two terms are calculated according to the GC-DFT method defined in the previous subsection (eq. 1). An example of the evolution of $G_{reactant}(U)$ is furnished in Fig. S1. $G_{Rmol}(U)$ is the energy of the adsorbing species. In the simplest case, the adsorbate is a water molecule, so that $G_{Rmol}(U)$ simply becomes 2 times G_{H_2O}, where the factor of two accounts for the symmetric nature of our systems.

For isolated molecules we use the following approximation for their free energy:

$$G_{mol} = E_{mol} - TS \tag{3}$$

where T is room temperature (298.15 K), and S is the contribution of rotational and translational entropy at standard pressure. For water, this entropy contribution is divided by two to account for its liquid state.[64,65] How to combine entropy, implicit solvent and dispersion corrections for water remains an actively debated subject.[66] In the present case, adsorption energies of water would be less exergonic by $\sim$0.3 eV if we would use the gas-phase entropy at 1 bar. Note that we have neglected vibrational contributions (thermal contributions and zero-point energy corrections) due to the large number of intermediates involved. This approximation was found to result in only small changes in our previous investigations.[67]

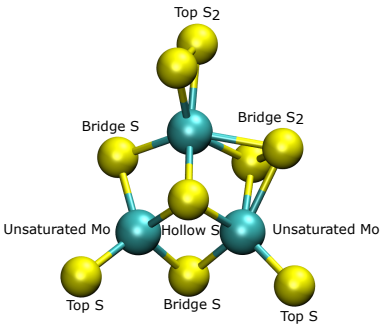

(a) Mo_3S_9 nano-cluster

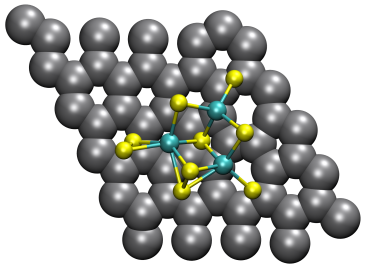

(b) Graphite with a Stone-Wales defect with adsorbed Mo_3S_9

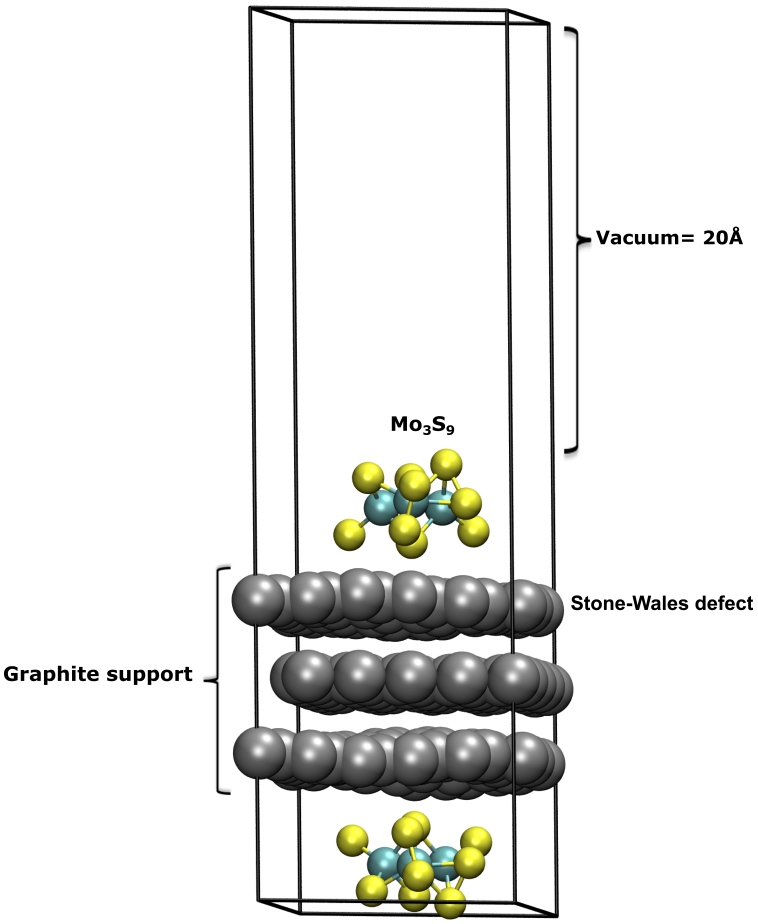

(c) Symmetric Mo_3S_9 on our graphite model

Figure 1: (a) Mo_3S_9 nanocluster with the labels of the atoms, (b) the top-most layer of graphite support with a Stone-Wales defect and Mo_3S_9 adsorbed and (c) symmetric Mo_3S_9 supported on graphite. The adsorption configuration shown is the most stable one. The color code for atoms is white for H; red for O; silver for C; yellow for S and greenish for Mo.

When investigating the *desorption* of H_2S, we determine the reverse of Eq. 2, with *Rmol* = 2 H_2S. G_{H_2S} is the free energy of the H_2S molecule at 1 bar. During HER the partial pressure of H_2S is very small (we could assume P_{H_2S}= 10^{-5} bar[68]), so even reactions that are endergonic (up to about 0.3 eV) at standard conditions have a reasonable probability of occurring under HER conditions.

When considering proton/electron transfers, the relevant adsorbate is related to H_2 via the computational hydrogen electrode approach.[69] Under standard conditions (pH = 0, T= 298 K, p = 1 bar) there is an equilibrium ($\Delta G = 0$) between hydrogen molecules in the gas phase and solvated protons and electrons at 0 V vs SHE:

$$H_{2(g)} \leftrightarrow 2 \times (H^+ + e^-) \tag{4}$$

Hence, the free energy of the H_2 molecule in the gas phase is used to determine the combined energy of $(H^+ + e^-)$:

$$2 \times (\mu_{H^+} + \mu_{e^-}) = G_{H_2} \tag{5}$$

When changing the potential away from 0 V versus SHE, a term eU has to be added to μ_{e^-} where e is the elementary charge and U the potential, all in suitable units.

Thus, when considering the symmetric adsorption of $H^+ + e^-$, i.e., the *Volmer* reaction, $G_{Rmol}(U)$ is defined as :

$$G_{Rmol}(U) = G_{H_{2(g)}} - 2eU \tag{6}$$

Note that following the generally applied convention, we will use H^++e^- when referring to a proton/electron pair. In the context of GC-DFT the electron transfer is not strictly coupled to the proton transfer and the electron transfer is often only "partial" on heterogeneous electrocatalysts (in contrast to molecular catalysts). Nevertheless, in all diagrams we will use the notation of $H^+ + e^-$, independent on the exact number of electrons (somewhere in

the range between 0 and 2, as shown later).

For the *Tafel* reaction, the situation is similar to the release of H_2S: *ads* is H_2 and we evaluate $-\Delta G_{ads}$.

The *Heyrovsky* reaction is a mixed case, formally equivalent to $-\Delta G_{ads}$ with $Rmol = H_2 - H^+ + e^-$, i.e.

$$\Delta G_{Heyrovsky}(U) = \frac{1}{2} \times (G_{surf}(U) - G_{surfH}(U) - 2G_{H^+ + e^-}(U) + 2G_{H2}) \tag{7}$$

where G_{surfH} is the energy of the system with one more adsorbed hydrogen compared to $surf$.

Similarly, when determining the formal adsorption of OH*, the energy of the adsorbing species under the relevant reducing conditions is $G_{Rmol}(U) = 2G_{\mathrm{H_2O}} + 2(H^+ + e^-) - 2G_{\mathrm{H_2}}$. In other words: OH* is formed by adsorption of H_2O followed by electroreduction (formally a Heyrovsky step), which releases H_2.

When a second adsorbate is adsorbed, the adsorption energy is calculated exactly as for the first adsorption, except that the initial surface ($G_{reactant}(U)$) already contains an adsorbate. Thus, the second adsorption energy is the differential adsorption energy.

Our previous studies[35,47] have shown that adsorbed OH* and H_2O species can participate in HER: OH* can be converted into H_2O via a Volmer-type reaction and H_2 can be released by a Heyrovsky-type reaction, i.e., a coupling of H from H_2O and $H^+ + e^-$ from the solution/electrode.

2.3 Identification of active sites

To identify the active sites for HER, we started from the Mo_3S_9 cluster without support (see section S2.1) and with the graphite supported (see section S2.2). The adsorption energies of H, OH, and H_2O were first computed in vacuum. All possible sites and the various phenomena such as the release of H_2 and H_2S were investigated. In the following sections,

we mainly discuss the most stable structures identified and the most promising sites, all revisited at the GC-DFT level. Furthermore, we have taken a "generative" approach, i.e., we have started from Mo_3S_9, have adsorbed species (H, H_2O) until reaching the most stable structure, determined the energetics for H_2S release and moved to the *thereby* generated Mo_3S_8 structure, for which we repeat the procedure to arrive at Mo_3S_7, which was found to be stable with respect to loss of H_2S. As a corollary of this overall approach, the determined coverages are most relevant around 0 V vs SHE, i.e., the equilibrium potential for HER. Significant changes in coverages (H, OH or H_2O) could occur at potentials far away from this reference potential. However, these coverages are irrelevant to the current study, which aims at investigating the active sites at low overpotentials, i.e., potentials close to 0 V.

3 Results and discussion

3.1 Instability of Mo_3S_9 in HER conditions

An important factor is the stability of the catalyst under HER conditions (here assumed to be strongly acidic, pH=0). As a first step we compute the hydrogen adsorption energies (ΔG_H) at the different possible active sites of Mo_3S_9 and the decomposition energy, i.e., the release of H_2S, which leads to possible reconstructions of the nanocluster (see section S3.1 in SI). As shown in the energy profile of Fig. S11, four hydrogen atoms could be adsorbed before the H_2S release takes place.

Since we are working in an aqueous medium, studying only hydrogen adsorption is not sufficient to assess the electrocatalytic activity of Mo_3S_9. Therefore, we also consider the adsorption of OH and H_2O. We have first computed the adsorption energies of H_2O and OH at the different possible sites without considering the electrochemical potential (see Fig. S4). The main conclusion is that OH* does not form, while one H_2O molecule adsorbs on each of the two unsaturated-Mo sites.

Based on these results, we proceeded to the grand-canonical DFT computations. Fig. 2

shows the corresponding energy profile starting with water adsorption, followed by hydrogen adsorption in the presence of the explicit water molecules. The first and second H_2O are adsorbed on the unsaturated-Mo sites with ΔG_{H_2O} equal to -0.16 eV and -0.14 eV, respectively. Then, the hydrogen adsorption follows the same path as in the absence of water molecules (Fig. S11). The first two H atoms are adsorbed on the two top S monomers. The third and fourth H atoms are located on one sulfur atom of the bridge S_2 species leading to the formation of H_2S molecule. The last step consists of the release of H_2S. The adsorption of the first, second and fourth hydrogen atoms are strongly exergonic with the differential ΔG_H equal to -0.62 eV, -0.60 eV and -0.45 eV, respectively. For the third hydrogen, the adsorption strength is only +0.28 eV. At this stage (Mo_3S_9_$2H_2O$_3H), the system can either perform HER (with an overpotential of about 0.2 eV) via a Heyrovsky mechanism, or an additional Volmer step (-0.45 eV) occurs. Once four hydrogens are adsorbed, the release of H_2S is exergonic (-0.16 eV). This value is calculated considering P_{H_2S}= 1 bar. Under HER conditions, we could assume a low partial pressure P_{H_2S}= 10^{-5} bar. At this pressure, the energy of H_2S release is -0.45 eV. As a result, the transformation of Mo_3S_9 into the Mo_3S_8_$2H_2O$_2H species is very likely under HER conditions. As a consequence, the HER activity of Mo_3S_8_$2H_2O$_2H is analyzed in the following.

3.2 HER catalyzed by sulfur species on Mo_3S_8 in presence of water

As in the previous subsection, we have first evaluated the energy profile at 0 V without the presence of water (see Fig. S12 in SI). Since the results of ΔG_{H_2O} showed that adsorption of two water molecules is favored on Mo_3S_8 (see Fig. S7 in SI), we focus here on the energy profile starting with Mo_3S_8_$2H_2O$_2H, i.e., the product obtained in the previous subsection. Like for Mo_3S_9, the hydrogen positions of Fig. 3 are not influenced by the presence of H_2O (compare to Fig. S12). The first adsorbed hydrogen is on one of the sulfur of the top S_2 dimer. Then, the second hydrogen adsorption occurs on the second sulfur of the top S_2 which induces the S-S bond breaking, leading to Mo_3S_8_$2H_2O$_4H containing 4 SH species in top

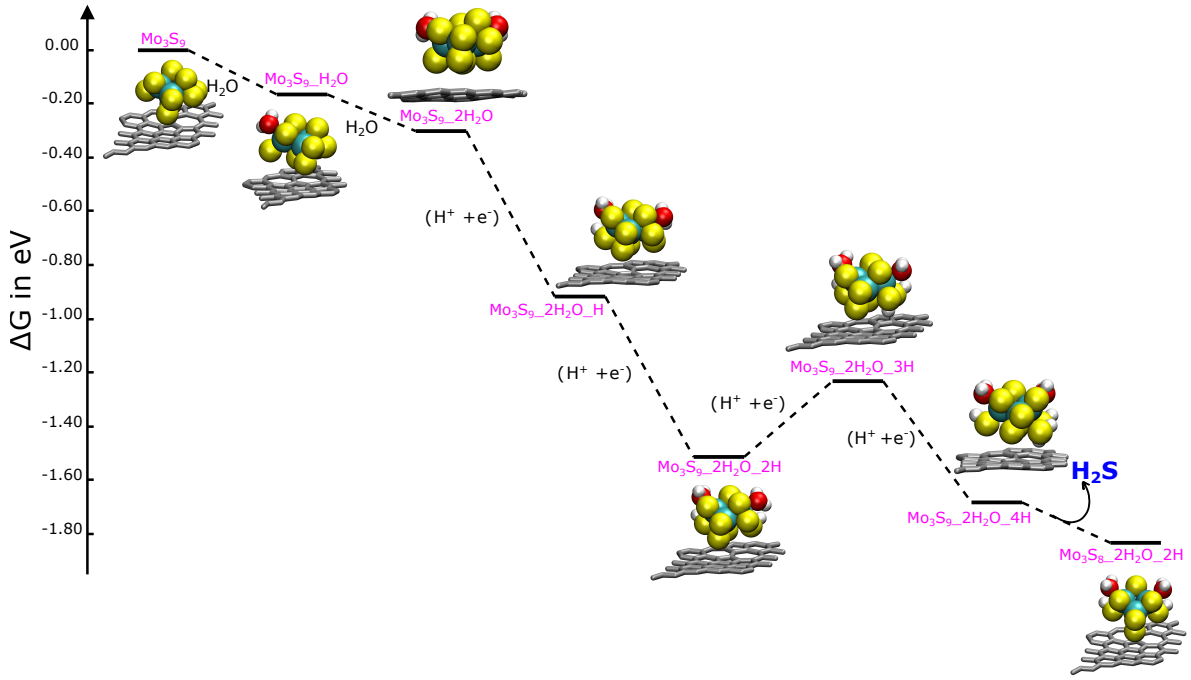

Figure 2: GC-DFT reaction energy profile on Mo_3S_9 at 0 V vs SHE. The first two steps correspond to water adsorptions. Then, the next four steps are hydrogen adsorptions and the last step is the release of H_2S. The color code for atoms is white for H; red for O; yellow for S and greenish for Mo. Note that here and in all following graphs we use the notation $H^+ + e^-$, independently on the actual (fractional) number of electrons that accompanies the proton transfer.

positions. From this lowest energy state (at 0 V vs SHE) of Fig. 3, the Tafel step corresponds to the transition from Mo_3S_8_$2H_2O$_4H "back" to Mo_3S_8_$2H_2O$_2H with production of H_2 and is endorgenic with an energy of +0.24 eV. Alternatively, the adsorption of another hydrogen to form H_2S is endergonic by only 0.13 eV.

From the produced Mo_3S_8_$2H_2O$_5H, three reactions must be analyzed: (i) the conversion of Mo_3S_8 to Mo_3S_7 upon H_2S release, (ii) the release of H_2 via a Heyrovsky mechanism, which corresponds to the transition of Mo_3S_8_$2H_2O$_5H "back" to Mo_3S_8_$2H_2O$_4H or (iii) a Tafel mechanism which is the transition from Mo_3S_8_$2H_2O$_5H to Mo_3S_8_$2H_2O$_3H. The H_2S release is endergonic by 0.43 eV at P_{H_2S}= 1 bar and 0.12 eV at $P_{H_2S} \approx 10^{-5}$ bar (close to HER conditions). While still endergonic, this process cannot be excluded, especially under long-term operating conditions with low H_2S partial pressures. The second scenario is the Heyrovsky mechanism which occurs with an energy equal to -0.13 eV. The configurations Mo_3S_8_$2H_2O$_5H and Mo_3S_8_$2H_2O$_4H involve Heyrovsky/Volmer steps with energies that are much closer to 0 eV than any configuration considered on the Mo_3S_9 clusters and are, therefore, good candidates for HER active sites. The last scenario, the Tafel step, occurs with a reaction energy of +0.23 eV.

In summary, during hydrogen adsorption on Mo_3S_8 in presence of water, different scenarios are possible. Energetically, the most favorable is the Heyrovsky step, then Tafel and the least probable is H_2S desorption. Hence, Mo_3S_8 is predicted to be HER active, with an overpotential close to 0 V (despite a slightly endergonic Volmer step, see Fig. 5) and slowly transforming into Mo_3S_7.

Regarding the nature of the active S-species involved in these Heyrovsky/Volmer steps, we find that the SH group located on top of the Mo atom that is formed after hydrogenation/dissociation of the top S_2 dimer has a central role. From this finding, we might infer that top S_2 dimer once hydrogenated could be key for HER activity. This differs from some interpretations earlier proposed in literature based on experimental considerations, and simultaneously agrees with others since an open debate is still present in the literature.[16–19]

Our result apparently does not support neither the proposal of MoS_2-edge-like sites with S^{2-} monomers[16] nor the one of bridging S_2^{2-} species to be active in HER.[18,20] By contrast, it seems consistent with the interpretation of Lassalle et al.[17] that top S_2 dimers lead to sulfhydryl as active species. However, since we also observed that Mo_3S_8_$2H_2O$_5H could release H_2S, this Mo_3S_8 based species may evolve to Mo_3S_7_$2H_2O$_3H which is further investigated in the following subsection.

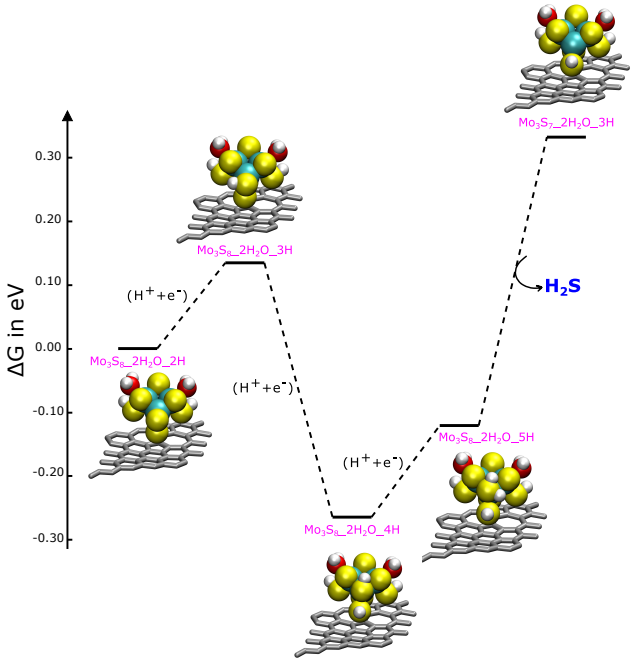

Figure 3: GC-DFT reaction energy profile on Mo_3S_8 at 0 V vs SHE. The first three steps correspond to hydrogen adsorption steps and the last step is the release of H_2S. The color code for atoms is white for H; red for O; yellow for S and greenish for Mo.

3.3 HER catalyzed by OH species on Mo_3S_7 in presence of water

In the present section, we investigate the reactivity of Mo_3S_7_$2H_2O$_3H (see Fig. 4). The desorption of H_2S from Mo_3S_8 generates an additional coordination unsaturated Mo site on Mo_3S_7_$2H_2O$_3H. Our computations show that the adsorption of water or OH are more favorable than hydrogen at this site (see Fig. S9). The fact that OH is the most favorable species for this adsorption site will have a specific impact on the HER mechanism (vide

infra). Having identified the possible adsorbates at the sulfur and molybdenum sites, we now study HER. The hydrogen atoms located on the top S atoms of Mo_3S_7 are all very strongly adsorbed ($\approx$ -1 eV). Therefore, their desorption through Heyrosvky or Tafel mechanisms is highly unlikely.

In our previous studies on MoS_2 edges, we have shown that water could be involved in hydrogen production.[47] The same concept was investigated here for Mo_3S_7. We found that only one H_2O of the three adsorbed water molecules could cycle with OH. As shown in Fig. 4, OH* formation is endergonic by 0.42 eV at 0 V, suggesting that it might be obtained under HER conditions via a Heyrovsky step, generating H_2. This was not possible with Mo_3S_9 and Mo_3S_8 as OH* is too unstable. The adsorbed OH* can then be reduced back to H_2O via an exergonic Volmer step with a reaction energy of -0.42 eV.

Our interpretation of the reactivity of Mo_3S_7 induced by OH groups can be fruitfully compared with some experimental results by Tran et al.[15] revealing that top S_2^{2-} species are eliminated and replaced by reactive oxygenated atoms. Also, other experimental studies invoked that the partial oxidation of the MoS_3 phase could be at the origin of the HER activity[33,34]

3.4 Potential dependence of Volmer and Heyrovsky steps and comparison of MoS_3 with MoS_2 catalysts

The literature suggests that MoS_3 may evolve towards the MoS_2 stoichiometry during HER[17] and that some active sites could be similar to MoS_2-edge sites.[16] Therefore, in the following we compare key computational results recently obtained[35] on MoS_2 with the same GC-DFT methodology as applied herein to the case of MoS_3. In this previous DFT study focusing on the MoS_2 electrocatalyst, MoS_2 edges were shown to be HER active despite possible edge reconstructions occurring under HER conditions.[35] For this comparison, we choose the Mo_3S_8 cluster because it represents a relevant working state for the amorphous MoS_3 phase, with the active sites involving sulfur atoms, in close analogy to the S-edge of MoS_2. Conversely,

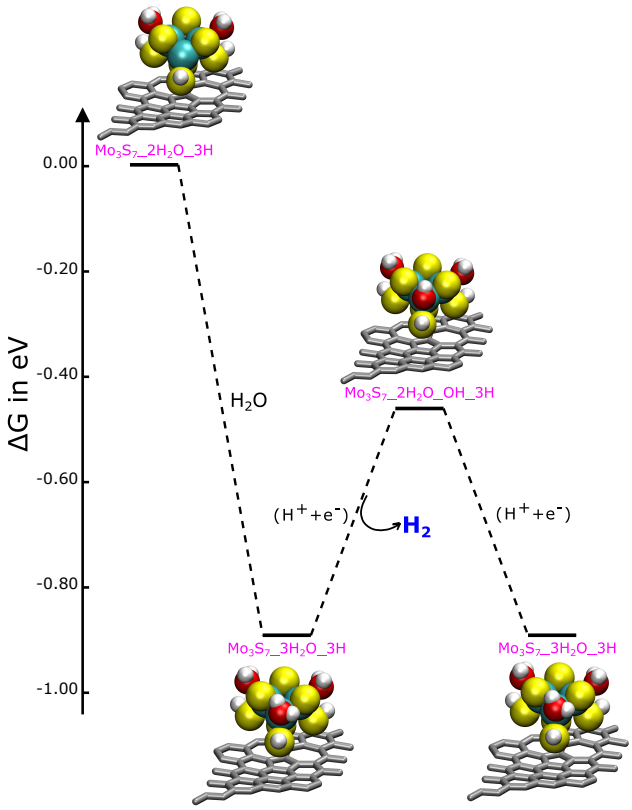

Figure 4: GC-DFT reaction energy profile on Mo_3S_7 at 0 V vs SHE. The first step corresponds to water adsorption, followed by a Heyrovsky step, and the last step is a Volmer step. The color code for atoms is white for H; red for O; yellow for S and greenish for Mo.

the Mo_3S_7 clusters are predicted to work via OH* groups, which resembles the case on the reconstructed Mo-edge of MoS_2.

Fig. 5a shows the variation of the Gibbs free energy for the Volmer and Heyrovsky steps occurring on MoS_2 S-edge and Mo_3S_8 as a function of the electrochemical potential, both invloving S atoms as active sites. As shown in Fig. 5b and Fig. 5c, the hydrogen adsorption via the Volmer reaction is potential-independent for Mo_3S_8, while it depends on the potential for MoS_2 S-edge case. In other words, it corresponds to a protonation, rather than a coupled proton electron transfer, which is an intriguing observation of a decoupled mechanism. This interpretation is verified by the analysis of the electron transfer as a function of the potential, which is close to 0 for a protonation step and close to 1 for a proton-coupled electron transfer, see Fig. S13. This difference between the two catalysts might be due to the different nature of S sites involved in H adsorption: top SH for Mo_3S_8 versus bridging S for MoS_2 S-edge. Alternatively, the difference of behavior could be related to the more localized (molecule-like) electronic structure of Mo_3S_8 featuring a "lone-pair", compared to the more delocalized electronic structure of MoS_2. The hydrogen production occurs via a Heyrovsky step involving a SH (sulfhydryl) group for MoS_2 and on a SH_2 (adsorbed H_2S) species for MoS_3. The release of H_2 is more strongly potential dependent for both catalysts compared to the Volmer step and involves about 1.8 and 1.1 electrons on MoS_3 and MoS_2, respectively. At 0 V vs SHE, we observe that Mo_3S_8 is more promising than the MoS_2 S-edge with ΔG_1 and ΔG_2 closer to 0 eV. However, the (slightly) endergonic protonation step required for Mo_3S_8 suggests that this catalyst will be more sensitive to changes in local pH than to changes in the electrochemical potential. Only for a more negative potential $\approx$ -0.3 V (where the Volmer step becomes exergonic), MoS_2 S-edge becomes active for HER.

According to our simulations on MoS_3, we cannot exclude that the S-active species may be lost through H_2S desorption. In this case, the active sites involve OH* entities, similar to the situation on the Mo-edge of MoS_2. Hence, we compare MoS_2 Mo-edge and Mo_3S_7 in Fig. 6. Fig. 6a shows the effects of the electrochemical potential on the Volmer and Heyrovsky

mechanisms for MoS_2 Mo-edge and Mo_3S_7, both involving OH* entities as the active sites, whereas water molecules or hydroxyls have only been spectators when the active sites where sulfur atoms. A more reducing electrochemical potential strongly favours the Heyrovsky step with the release of H_2 particularly for Mo_3S_7, i.e., the formation of OH* is very close to 0 eV at -0.2 V vs SHE. We find again that the "Volmer" step on Mo_3S_7 is potential independent and remains close to -0.4 eV, and is thus best understood as a protonation step, as confirmed by the analysis of the charge, see Fig. S14. The main difference with the active sites on Mo_3S_8 is that the oxygen atom of the top OH species is more basic than the sulfur atom of the top SH* group and, therefore, the protonation is exergonic for Mo_3S_7. This protonation step is also in line with the strong slope of nearly 2 eV/V of the Heyrovsky step as a function of the electrochemical potential. This observation of a decoupled electron and proton transfer is rare in electrocatalysis. We conclude that water and the explicit incorporation of the electrochemical potential play an important role in the hydrogen evolution reaction on Mo_3S_7. In contrast to the previous case, the MoS_2 Mo-edge is more promising than Mo_3S_7 with a thermodynamic overpotential close to 0 V.

In summary, all reported MoS_2 and MoS_3 structures are catalytically active for HER. However, their optimal working regimes depend on the active sites involved. Note that modelling the solvent effects more explicitly (e.g., via QM/MM[70] or DFT-based molecular dynamics[71,72]) would provide an even more comprehensive understanding, especially if coupled to the computationally expensive determination of transition states.[59,73–75] When hydrogen release involves SH site on Mo_3S_8 cluster, MoS_3 is more promising. By contrast, MoS_2 is more promising when water is involved and hydrogen release occurs via OH sites located on the Mo-edge. This trend might provide some explanations on experimental observations reporting that MoS_2 (either amorphous or crystalline) might be formed from MoS_3 during HER and provide the HER activity.[16,17] According to our analysis, this can only be due to the formation of active Mo-edge involving top OH* species. This interpretation slightly differs from the ones proposed in[16,17] where only pure sulfided species are invoked

to be active.

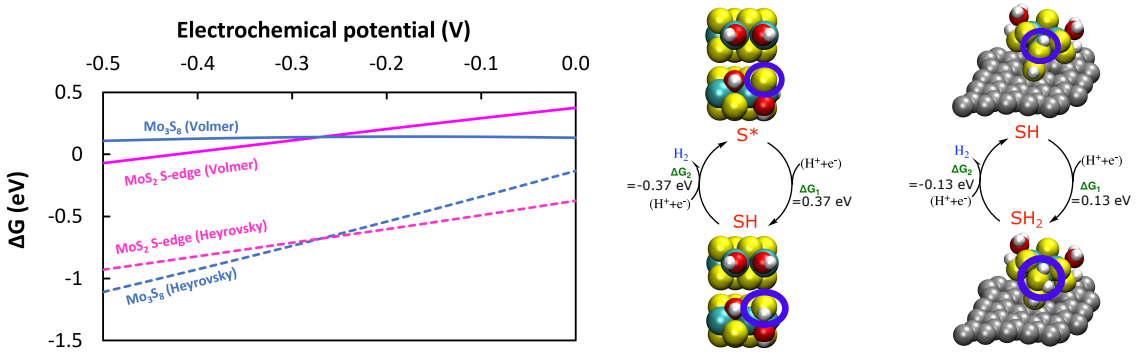

(a) (b) MoS_2 S-edge (c) Mo_3S_8

Figure 5: (a) Variation of ΔG_1, the Volmer step and ΔG_2, the Heyrovsky step as a function of the electrochemical potential for MoS_2 S-edge and Mo_3S_8, (b) the cycle between SH and S to release H_2 on MoS_2 S-edge at 0 V and (c) the cycle between SH_2 and SH to release H_2 on Mo_3S_8 at 0 V. The color code for atoms is white for H; red for O; silver for C; yellow for S and greenish for Mo. See Fig. S13 for the quantification of the number of electrons that are transferred together with the protons.

4 Conclusion

We have performed state-of-the-art grand-canonical DFT computations relying on a cluster-continuum solvation strategy and applied them to Mo_3S_{9-x} cluster models of the MoS_3 electrocatalytically active phase supported on carbon. We determined systematically the thermodynamic profiles of hydrogen adsorption and H_2 production by taking into account the stability of the catalyst with respect to H_2O adsorption and H_2S desorption. The chemically adsorbed water molecules are treated explicitly, while the bulk effect of the solvent and the electrolyte are described via the linearized Poisson-Boltzmann equation.

Our approach enabled to identify that the starting Mo_3S_9 cluster is not stable in HER conditions and may evolve to a Mo_3S_8 or even Mo_3S_7 based clusters after H_2S releases. Both clusters also contain adsorbed water molecules and OH species adsorbed on the unsaturated Mo sites that cauterize the Mo coordination sphere. The Mo_3S_8 cluster containing two water molecules is found to be active in HER through Heyrovsky-Volmer mechanisms involving

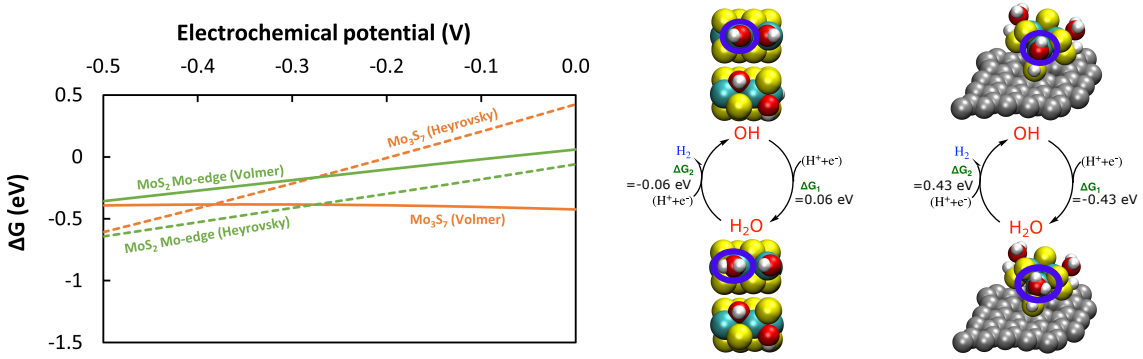

(a) (b) MoS_2 Mo-edge (c) Mo_3S_7

Figure 6: (a) Variation of ΔG_1, the Volmer step and ΔG_2, the Heyrovsky step as a function of the electrochemical potential for MoS_2 Mo-edge and Mo_3S_7, (b) the cycle between H_2O and OH to release H_2 on MoS_2 Mo-edge at 0 V and (c) the cycle between H_2O and OH to release H_2 on Mo_3S_7 at 0 V. The color code for atoms is white for H; red for O; silver for C; yellow for S and greenish for Mo. See Fig. S14 for the quantification of the number of electrons that are transferred together with the protons.

top SH* species resulting from the hydrogenation of a top S_2^{2-} dimer. They are predicted to be catalytically more active than the bridging SH* sites located on the S-edge of a MoS_2 electrocatalyst. The Mo_3S_7 clusters containing two water molecules and one OH* group is also active in HER even if less than the Mo_3S_8 cluster and than the Mo-edge of a MoS_2 electrocatalyst. The Herovsky/Volmer mechanisms involves the OH* species and leads to a thermodynamic overpotential of about 0.2 V.

Moreover, we found that the HER mechanism on Mo_3S_8 and Mo_3S_7 clusters involves a potential independent protonation step, which does not follow the common coupled proton electron transfer.

In summary, our DFT study highlights the versatile working state and reactivity of carbon supported Mo_3S_{9-x} clusters in HER conditions. Depending on the impact of water and sulfur resilience, the HER activity may originate either from SH* or OH* groups which may help to rationalize the open debate reported in the experimental literature regarding the nature of HER active sites. This study also provides a consistent comparison of the HER reactivity of MoS_3 and MoS_2 electrocatalysts.

Acknowledgement

This work was financially supported by Région Auvergne Rhône-Alpes through the project Pack Ambition Recherche 2018 MoSHi. It is also a part of the "RatiOnAl Design for CATalysis" (ROAD4CAT) industrial chair, project IDEXLYON funded by the French National Research Agency (ANR-16-IDEX-0005) and the Commissariat-General for Investment (CGI) within the framework of Investissements d'Avenir program ("Investment for the future"). We are very grateful to IFP Energies nouvelles for supporting the MoSHy project (N^o 1801167601) and to the IFP Energies nouvelles team, Mona Marie Obadia and Quentin Cacciuttolo, for hydrogen production by water electrolysis. We thank Danish Pannu for the construction of the Stone-Wales defect containing carbon model. The authors thank the SYSPROD project and AXELERA Pôle de Compétitivité for financial support (PSMN Data Center).

Supporting Information Available

The Supporting Information is available free of charge at `https://pubs.acs.org/doi/10.1021/xxx` Additional Figures and Tables related to computations in vacuum and in the absence of chemisorbed water molecules (PDF). The coordinates of all symmetric zero-charge systems investigated herein are freely available under: `http://doi.org/10.17172/NOMAD/2023.07.18-1`.

References

(1) Gür, T. M. Review of electrical energy storage technologies, materials and systems: challenges and prospects for large-scale grid storage. *Energy & Environmental Science* **2018**, *11*, 2696–2767.

(2) Singh, S.; Jain, S.; Venkateswaran, P.; Tiwari, A. K.; Nouni, M. R.; Pandey, J. K.;

Goel, S. Hydrogen: A sustainable fuel for future of the transport sector. *Renewable and sustainable energy reviews* **2015**, *51*, 623–633.

(3) Andrews, J.; Shabani, B. The role of hydrogen in a global sustainable energy strategy. *Wiley Interdisciplinary Reviews: Energy and Environment* **2014**, *3*, 474–489.

(4) Singla, M. K.; Nijhawan, P.; Oberoi, A. S. Hydrogen fuel and fuel cell technology for cleaner future: a review. *Environmental Science and Pollution Research* **2021**, *28*, 15607–15626.

(5) Yu, M.; Wang, K.; Vredenburg, H. Insights into low-carbon hydrogen production methods: Green, blue and aqua hydrogen. *International Journal of Hydrogen Energy* **2021**, *46*, 21261–21273.

(6) Holladay, J. D.; Hu, J.; King, D. L.; Wang, Y. An overview of hydrogen production technologies. *Catalysis today* **2009**, *139*, 244–260.

(7) Zou, X.; Zhang, Y. Noble metal-free hydrogen evolution catalysts for water splitting. *Chemical Society Reviews* **2015**, *44*, 5148–5180.

(8) McCrory, C. C.; Jung, S.; Ferrer, I. M.; Chatman, S. M.; Peters, J. C.; Jaramillo, T. F. Benchmarking hydrogen evolving reaction and oxygen evolving reaction electrocatalysts for solar water splitting devices. *Journal of the American Chemical Society* **2015**, *137*, 4347–4357.

(9) Chen, R.; Yang, C.; Cai, W.; Wang, H.-Y.; Miao, J.; Zhang, L.; Chen, S.; Liu, B. Use of platinum as the counter electrode to study the activity of nonprecious metal catalysts for the hydrogen evolution reaction. *ACS energy letters* **2017**, *2*, 1070–1075.

(10) Vrubel, H.; Merki, D.; Hu, X. Hydrogen evolution catalyzed by MoS_3 and MoS_2 particles. *Energy & Environmental Science* **2012**, *5*, 6136–6144.

(11) Benck, J. D.; Hellstern, T. R.; Kibsgaard, J.; Chakthranont, P.; Jaramillo, T. F. Catalyzing the hydrogen evolution reaction (HER) with molybdenum sulfide nanomaterials. *ACS Catalysis* **2014**, *4*, 3957–3971.

(12) Escalera-López, D.; Lou, Z.; Rees, N. V. Benchmarking the activity, stability, and inherent electrochemistry of amorphous molybdenum sulfide for hydrogen production. *Advanced Energy Materials* **2019**, *9*, 1802614.

(13) Wu, L.; Longo, A.; Dzade, N. Y.; Sharma, A.; Hendrix, M. M. R. M.; Bol, A. A.; de Leeuw, N. H.; Hensen, E. J. M.; Hofmann, J. P. The Origin of High Activity of Amorphous MoS_2 in the Hydrogen Evolution Reaction. *ChemSusChem* **2019**, *12*, 4383–4389.

(14) Benck, J. D.; Chen, Z.; Kuritzky, L. Y.; Forman, A. J.; Jaramillo, T. F. Amorphous molybdenum sulfide catalysts for electrochemical hydrogen production: insights into the origin of their catalytic activity. *Acs Catalysis* **2012**, *2*, 1916–1923.

(15) Tran, P. D.; Tran, T. V.; Orio, M.; Torelli, S.; Truong, Q. D.; Nayuki, K.; Sasaki, Y.; Chiam, S. Y.; Yi, R.; Honma, I., et al. Coordination polymer structure and revisited hydrogen evolution catalytic mechanism for amorphous molybdenum sulfide. *Nature materials* **2016**, *15*, 640–646.

(16) Casalongue, H. G. S.; Benck, J. D.; Tsai, C.; Karlsson, R. K.; Kaya, S.; Ng, M. L.; Pettersson, L. G.; Abild-Pedersen, F.; Nørskov, J.; Ogasawara, H., et al. Operando characterization of an amorphous molybdenum sulfide nanoparticle catalyst during the hydrogen evolution reaction. *The Journal of Physical Chemistry C* **2014**, *118*, 29252–29259.

(17) Lassalle-Kaiser, B.; Merki, D.; Vrubel, H.; Gul, S.; Yachandra, V. K.; Hu, X.; Yano, J. Evidence from in situ X-ray absorption spectroscopy for the involvement of terminal

disulfide in the reduction of protons by an amorphous molybdenum sulfide electrocatalyst. *Journal of the American Chemical Society* **2015**, *137*, 314–321.

(18) Deng, Y.; Ting, L. R. L.; Neo, P. H. L.; Zhang, Y.-J.; Peterson, A. A.; Yeo, B. S. Operando Raman spectroscopy of amorphous molybdenum sulfide (MoS_x) during the electrochemical hydrogen evolution reaction: Identification of sulfur atoms as catalytically active sites for H+ reduction. *ACS catalysis* **2016**, *6*, 7790–7798.

(19) Li, Y.; Nakamura, R. Structural change of molybdenum sulfide facilitates the electrocatalytic hydrogen evolution reaction at neutral pH as revealed by in situ Raman spectroscopy. *Chinese Journal of Catalysis* **2018**, *39*, 401–406.

(20) Chang, Y.-H.; Lin, C.-T.; Chen, T.-Y.; Hsu, C.-L.; Lee, Y.-H.; Zhang, W.; Wei, K.-H.; Li, L.-J. Highly Efficient Electrocatalytic Hydrogen Production by MoS_x Grown on Graphene-Protected 3D Ni Foams. *Advanced Materials* **2013**, *25*, 756–760.

(21) Sahu, A.; Steinmann, S. N.; Raybaud, P. Size-Dependent Structural, Energetic, and Spectroscopic Properties of MoS_3 Polymorphs. *Crystal Growth & Design* **2020**, *20*, 7750–7760.

(22) Liang, K.; Cramer, S.; Johnston, D.; Chang, C.; Jacobson, A.; Deneufville, J.; Chianelli, R. Amorphous MoS_3 and WS_3. *Journal of Non-Crystalline Solids* **1980**, *42*, 345–356.

(23) Weber, T.; Muijsers, J.; Niemantsverdriet, J. Structure of amorphous MoS_3. *The Journal of Physical Chemistry* **1995**, *99*, 9194–9200.

(24) Hibble, S. J.; Walton, R. I.; Pickup, D. M.; Hannon, A. C. Amorphous MoS_3: clusters or chains? The structural evidence. *Journal of non-crystalline solids* **1998**, *232*, 434–439.

(25) Jiao, H.; Li, Y.-W.; Delmon, B.; Halet, J.-F. The structure and possible catalytic sites

of Mo_3S_9 as a model of amorphous molybdenum trisulfide: a computational study. *Journal of the American Chemical Society* **2001**, *123*, 7334–7339.

(26) Kibsgaard, J.; Jaramillo, T. F.; Besenbacher, F. Building an appropriate active-site motif into a hydrogen-evolution catalyst with thiomolybdate $[Mo_3S_{13}]^{2-}$ clusters. *Nature Chem* **2014**, *6*, 248–253.

(27) Huang, Z.; Luo, W.; Ma, L.; Yu, M.; Ren, X.; He, M.; Polen, S.; Click, K.; Garrett, B.; Lu, J., et al. Dimeric $[Mo_2S_{12}]^{2-}$ cluster: a molecular analogue of MoS_2 edges for superior hydrogen-evolution electrocatalysis. *Angewandte chemie international edition* **2015**, *54*, 15181–15185.

(28) Lei, Y.; Yang, M.; Hou, J.; Wang, F.; Cui, E.; Kong, C.; Min, S. Thiomolybdate $[Mo_3S_{13}]^{2-}$ nanocluster: a molecular mimic of MoS_2 active sites for highly efficient photocatalytic hydrogen evolution. *Chemical Communications* **2018**, *54*, 603–606.

(29) Rajagopal, A.; Venter, F.; Jacob, T.; Petermann, L.; Rau, S.; Tschierlei, S.; Streb, C. Homogeneous visible light-driven hydrogen evolution by the molecular molybdenum sulfide model $[Mo_2S_{12}]^{2-}$. *Sustainable energy & fuels* **2019**, *3*, 92–95.

(30) Dave, M.; Rajagopal, A.; Damm-Ruttensperger, M.; Schwarz, B.; Naegele, F.; Daccache, L.; Fantauzzi, D.; Jacob, T.; Streb, C. Understanding homogeneous hydrogen evolution reactivity and deactivation pathways of molecular molybdenum sulfide catalysts. *Sustainable Energy & Fuels* **2018**, *2*, 1020–1026.

(31) Ting, L. R. L.; Deng, Y.; Ma, L.; Zhang, Y.-J.; Peterson, A. A.; Yeo, B. S. Catalytic activities of sulfur atoms in amorphous molybdenum sulfide for the electrochemical hydrogen evolution reaction. *Acs Catalysis* **2016**, *6*, 861–867.

(32) Li, Y.; Yu, Y.; Huang, Y.; Nielsen, R. A.; Goddard III, W. A.; Li, Y.; Cao, L. Engineering the composition and crystallinity of molybdenum sulfide for high-performance electrocatalytic hydrogen evolution. *ACS catalysis* **2015**, *5*, 448–455.

(33) Sera, Y.; Seto, S.; Isobe, K.; Hashimoto, H. Development of highly active hydrogen evolution reaction (HER) catalysts composed of reduced graphene oxide and amorphous molybdenum sulfides derived from $(NH_4)_2MoO_{4-m}S_{4-m}$ (m= 0, 1, and 2). *Journal of Photochemistry and Photobiology A: Chemistry* **2020**, *401*, 112793.

(34) Giuffredi, G.; Mezzetti, A.; Perego, A.; Mazzolini, P.; Prato, M.; Fumagalli, F.; Lin, Y.-C.; Liu, C.; Ivanov, I. N.; Belianinov, A., et al. Non-Equilibrium Synthesis of Highly Active Nanostructured, Oxygen-Incorporated Amorphous Molybdenum Sulfide HER Electrocatalyst. *Small* **2020**, *16*, 2004047.

(35) Abidi, N.; Bonduelle-Skrzypczak, A.; Steinmann, S. N. How Stable Are 2H-MoS_2 Edges under Hydrogen Evolution Reaction Conditions? *The Journal of Physical Chemistry C* **2021**, *125*, 17058–17067.

(36) Sahu, A.; Steinmann, S. N.; Raybaud, P. Genesis of MoS_2 from model-Mo-oxide precursors supported on γ-alumina. *Journal of Catalysis* **2022**, *408*, 303–315.

(37) Payen, E.; Kasztelan, S.; Houssenbay, S.; Szymanski, R.; Grimblot, J. Genesis and characterization by laser Raman spectroscopy and high-resolution electron microscopy of supported molybdenum disulfide crystallites. *The Journal of Physical Chemistry* **1989**, *93*, 6501–6506.

(38) Morales-Guio, C. G.; Hu, X. Amorphous molybdenum sulfides as hydrogen evolution catalysts. *Accounts of chemical research* **2014**, *47*, 2671–2681.

(39) Kresse, G.; Furthmüller, J. Efficient iterative schemes for ab initio total-energy calculations using a plane-wave basis set. *Physical review B* **1996**, *54*, 11169.

(40) Perdew, J. P.; Burke, K.; Ernzerhof, M. Generalized gradient approximation made simple. *Physical review letters* **1996**, *77*, 3865.

(41) Steinmann, S. N.; Corminboeuf, C. Comprehensive benchmarking of a density-dependent dispersion correction. *Journal of chemical theory and computation* **2011**, *7*, 3567–3577.

(42) Blöchl, P. E. Projector augmented-wave method. *Physical review B* **1994**, *50*, 17953.

(43) Kresse, G.; Joubert, D. From ultrasoft pseudopotentials to the projector augmented-wave method. *Physical review b* **1999**, *59*, 1758.

(44) Martí, C.; Blanck, S.; Staub, R.; Loehlé, S.; Michel, C.; Steinmann, S. N. DockOnSurf: a python code for the high-throughput screening of flexible molecules adsorbed on surfaces. *Journal of Chemical Information and Modeling* **2021**, *61*, 3386–3396.

(45) Mathew, K.; Kolluru, V. S. C.; Mula, S.; Steinmann, S. N.; Hennig, R. G. Implicit self-consistent electrolyte model in plane-wave density-functional theory. *J. Chem. Phys.* **2019**, *151*, 234101.

(46) Steinmann, S. N.; Michel, C.; Schwiedernoch, R.; Sautet, P. Impacts of electrode potentials and solvents on the electroreduction of CO_2: A comparison of theoretical approaches. *Physical Chemistry Chemical Physics* **2015**, *17*, 13949–13963.

(47) Abidi, N.; Bonduelle-Skrzypczak, A.; Steinmann, S. N. Revisiting the Active Sites at the MoS_2/H_2O Interface via Grand-Canonical DFT: The Role of Water Dissociation. *ACS Appl. Mater. Interfaces* **2020**, *12*, 31401–31410.

(48) Abidi, N.; Bonduelle-Skrzypczak, A.; Steinmann, S. N. Potential and support-dependent hydrogen evolution reaction activation energies on sulfur vacancies of MoS_2 from GC-DFT. *Int. J. Hydrog. Energy* **2023**, *48*, 8478–8488.

(49) Steinmann, S. N.; Sautet, P. Assessing a first-principles model of an electrochemical interface by comparison with experiment. *J. Phys. Chem. C* **2016**, *120*, 5619–5623.

(50) Jinnouchi, R.; Anderson, A. B. Electronic structure calculations of liquid-solid interfaces: Combination of density functional theory and modified Poisson-Boltzmann theory. *Phys. Rev. B* **2008**, *77*, 245417.

(51) Fang, Y.-H.; Liu, Z.-P. Mechanism and Tafel Lines of Electro-Oxidation of Water to Oxygen on RuO_2(110). *J. Am. Chem. Soc.* **2010**, *132*, 18214–18222.

(52) Letchworth-Weaver, K.; Arias, T. A. Joint density functional theory of the electrode-electrolyte interface: Application to fixed electrode potentials, interfacial capacitances, and potentials of zero charge. *Phys. Rev. B* **2012**, *86*, 075140.

(53) Sundararaman, R.; Goddard, W. A.; Arias, T. A. Grand canonical electronic density-functional theory: Algorithms and applications to electrochemistry. *J. Chem. Phys.* **2017**, *146*, 114104.

(54) Zhang, H.; Goddard, W. A.; Lu, Q.; Cheng, M.-J. The importance of grand-canonical quantum mechanical methods to describe the effect of electrode potential on the stability of intermediates involved in both electrochemical CO_2 reduction and hydrogen evolution. *Phys. Chem. Chem. Phys.* **2018**, *20*, 2549–2557.

(55) Hörmann, N. G.; Andreussi, O.; Marzari, N. Grand canonical simulations of electrochemical interfaces in implicit solvation models. *J. Chem. Phys.* **2019**, *150*, 041730.

(56) Nalewajski, R. F.; Parr, R. G. Legendre Transforms and Maxwell Relations in Density Functional Theory. *J. Chem. Phys.* **1982**, *77*, 399–407.

(57) GoldBook, Standard Hydrogen electrode, `http://goldbook.iupac.org/S05917.html`.

(58) Melander, M. M.; Kuisma, M. J.; Christensen, T. E. K.; Honkala, K. Grand-canonical approach to density functional theory of electrocatalytic systems: Thermodynamics of

solid-liquid interfaces at constant ion and electrode potentials. *J. Chem. Phys.* **2019**, *150*, 041706.

(59) Melander, M. M. Grand canonical ensemble approach to electrochemical thermodynamics, kinetics, and model Hamiltonians. *Curr. Opin. Electrochem.* **2021**, 100749.

(60) Curutchet, A.; Colinet, P.; Michel, C.; Steinmann, S. N.; Le Bahers, T. Two-sites are better than one: revisiting the OER mechanism on CoOOH by DFT with electrode polarization. *Physical Chemistry Chemical Physics* **2020**, *22*, 7031–7038.

(61) Shang, R.; Steinmann, S. N.; Xu, B.-Q.; Sautet, P. Mononuclear Fe in N-doped carbon: computational elucidation of active sites for electrochemical oxygen reduction and oxygen evolution reactions. *Catal. Sci. Technol.* **2020**, *10*, 1006–1014.

(62) Hajar, Y. M.; Treps, L.; Michel, C.; Baranova, E. A.; Steinmann, S. N. Theoretical insight into the origin of the electrochemical promotion of ethylene oxidation on ruthenium oxide. *Catalysis Science and Technology* **2019**, *9*, 5915–5926.

(63) Panaritis, C.; Hajar, Y. M.; Treps, L.; Michel, C.; Baranova, E. A.; Steinmann, S. N. Demystifying the Atomistic Origin of the Electric Field Effect on Methane Oxidation. *J. Phys. Chem. Lett.* **2020**, *11*, 6976–6981.

(64) Deubel, D. V.; Lau, J. K.-c. In silico evolution of substrate selectivity : comparison of organometallic ruthenium complexes with the anticancer drug cisplatin . **2006**, *2*, 2451–2453.

(65) Kua, J.; Thrush, K. L. HCN, Formamidic Acid, and Formamide in Aqueous Solution: A Free-Energy Map. *J. Phys. Chem. B* **2016**, *120*, 8175–8185.

(66) Besora, M.; Vidossich, P.; Lledós, A.; Ujaque, G.; Maseras, F. Calculation of Reaction Free Energies in Solution: A Comparison of Current Approaches. *J. Phys. Chem. A* **2018**, *122*, 1392–1399.

(67) Abidi, N.; Bonduelle-Skrzypczak, A.; Steinmann, S. N. How to dope the basal plane of 2H-MoS_2 to boost the hydrogen evolution reaction? *Electrochim. Acta* **2023**, *439*, 141653.

(68) Tsai, C.; Chan, K.; Abild-Pedersen, F.; Nørskov, J. K. Active edge sites in $MoSe_2$ and WSe_2 catalysts for the hydrogen evolution reaction: a density functional study. *Phys. Chem. Chem. Phys.*

(69) Nørskov, J. K.; Rossmeisl, J.; Logadottir, A.; Lindqvist, L. R. K. J.; Kitchin, J. R.; Bligaard, T.; Jonsson, H. Origin of the overpotential for oxygen reduction at a fuel-cell cathode. *J. Phys. Chem. B* **2004**, *108*, 17886–17892.

(70) Abidi, N.; Steinmann, S. N. An Electrostatically Embedded QM/MM Scheme for Electrified Interfaces. *ACS Appl. Mater. Interfaces* **2023**, *15*, 25009–25017.

(71) Bonnet, N.; Morishita, T.; Sugino, O.; Otani, M. First-Principles Molecular Dynamics at a Constant Electrode Potential. *Phys. Rev. Lett.* **2012**, *109*, 266101–.

(72) Groß, A. Challenges for ab initio molecular dynamics simulations of electrochemical interfaces. *Current Opinion in Electrochemistry* **2023**, *40*, 101345.

(73) Huang, Y.; Nielsen, R. J.; Goddard III, W. A.; Soriaga, M. P. The reaction mechanism with free energy barriers for electrochemical dihydrogen evolution on MoS_2. *J. Am. Chem. Soc.* **2015**, *137*, 6692–6698.

(74) Huang, Y.; Nielsen, R. J.; Goddard III, W. A. Reaction Mechanism for the Hydrogen Evolution Reaction on the Basal Plane Sulfur Vacancy Site of MoS_2 Using Grand Canonical Potential Kinetics. *Journal of the American Chemical Society* **2018**, *140*, 16773–16782.

(75) Abidi, N.; Steinmann, S. N. How are Transition States Modelled in Heterogeneous Electrocatalysis? *Curr. Opin. Electrochem.* **2022**, *33*, 100940.

TOC Graphic

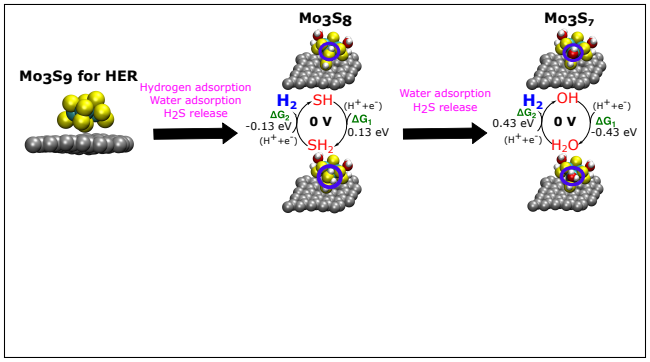
Mo3S9 for HER
Hydrogen adsorption
Water adsorption
H2S release
Mo3S8
H2
SH
SH2
ΔG2
-0.13 eV
(H+ +e-)
0 V
ΔG1
0.13 eV
(H+ +e-)
Water adsorption
H2S release
Mo3S7
H2
OH
H2O
ΔG2
0.43 eV
(H+ +e-)
0 V
ΔG1
-0.43 eV
(H+ +e-)